ChemCatChem

Research Article
doi.org/10.1002/cctc.202300647

Chemistry Europe
European Chemical Societies Publishing

www.chemcatchem.org

Black Phosphorus as Promoter for Noble Metal-Free Photocatalytic Hydrogen Production

Giacomo Provinciali,[a, b] Jonathan Filippi,[a] Alessandro Lavacchi,[a] Stefano Caporali,[c] Martina Banchelli,[d] Manuel Serrano-Ruiz,[a] Maurizio Peruzzini,[a] and Maria Caporali*[a]

Photocatalysts which are stable to photocorrosion and noble metal-free, are highly desirable to achieve a light-driven hydrogen production which satisfies the criteria of low production cost and environmental sustainability. Herein, a new heterostructure TiO_2/BP/CoP has been developed, in which the BP nanosheets interact strongly with TiO_2 and CoP, speeding up the transfer of photogenerated electrons and thus increasing H_2 production. Once BP is added to TiO_2 (P25) as only 1 %wt., the H_2 evolution rate increases up to 4 times reaching a value of 830 μmol/g·h under UV-Vis light irradiation. By integrating CoP nanoparticles as a cocatalyst up to 2 %wt., H_2 production is further promoted to 7400 μmol/g·h, 37 times higher than pristine TiO_2. Photoluminescence and electrochemical impedance measurements show that this heterostructure achieves a much more efficient charge separation and reduction of the internal resistance in comparison to pristine TiO_2. Combining these data with UV-Vis diffuse reflectance and Mott-Schottky, a plausible mechanism was proposed.

Introduction

One of the main challenges of our society is the development and use of clean energy that circumvents the exploitation of traditional fossil fuels. On this scenario, H_2 is one of the cleanest and most promising energy vector having high-energy capacity of 143 MJ kg^{-1}, which is much higher than common fossil fuels, and has also emission-free feature.[1] However, the large amount of H_2 required by the chemical industry is produced nowadays mainly by steam reforming of hydrocarbons[2] where unfortunately a substantial amount of CO_2 is generated. Renewable sources are at earlier stage of development, among them an appealing choice for the production of green H_2 is the process of photocatalytic water splitting using solar energy, being the latter one of the most promising renewable and clean energy sources. Other cutting-the-edge processes as CO_2 reduction[3] and waste water remediation[4] aim to use solar power to drive the chemical reaction, in principle photocatalysis is forecasted as a powerful technology but before being largely used, requires the discovery of highly performing photocatalysts able to transform efficiently the solar into chemical energy.

Following the pioneering study of water splitting over a TiO_2 electrode in 1972,[5] titanium dioxide is largely investigated as photocatalyst for H_2 production, since it is not toxic, relatively cheap and endowed with excellent stability under photochemical conditions. As drawbacks, TiO_2 is a wide band gap semiconductor ($E_g = 3.0–3.3$ eV), thus works only under UV-light and presents a relatively fast electron-hole recombination rate.[6] To overcome these problems, common strategies are i) building a type-II band alignment heterojunction by coupling TiO_2 with a suitable semiconductor that absorbs in the visible region,[7,8] ii) usage of a co-catalyst loading.[9] In conjunction with this and in the frame of a sustainable development, the goal is also to improve the catalysis by replacing a metal with a non-metal element, which in principle is more abundant and less toxic. On this regard, several studies have involved elemental phosphorus in particular the red allotrope, as semiconductor in photocatalytic processes.[10,11] Only recently, bidimensional black phosphorus (BP) has attracted an increasing attention being a semiconductor with high carrier mobility (up to 1000 $cm^2 V^{-1} s^{-1}$ at RT) and narrow band gap that can be modulated and goes from 0.3 eV in the bulk to 2.0 eV in the monolayer.[12] This means BP can absorb light in the spectral range from visible to near IR and thus it is highly suitable for the construction of wide spectral responsive photocatalysts, additionally it is endowed with a conduction band much more negative than the redox potential of H^+/H_2 couple that makes it a good candidate for solar–driven H_2 generation from water. Since the seminal work of H. Ji's group[13] in 2017 who demonstrated that hydroxyl functionalized BP nanosheets can produce H_2 once irradiated by visible light, with an evolution rate of 512 μmol/g·h, several efforts have been done to design

[a] G. Provinciali, J. Filippi, A. Lavacchi, M. Serrano-Ruiz, M. Peruzzini, Dr. M. Caporali
CNR-ICCOM
Via Madonna del Piano 10, 5019 Sesto Fiorentino (Italy)
E-mail: maria.caporali@iccom.cnr.it

[b] G. Provinciali
Department of Chemical Sciences
University of Padua
35131 Padua (Italy)

[c] S. Caporali
Department of Industrial Engineering
University of Florence
Via di S. Marta 3, 50139 Firenze (Italy)

[d] M. Banchelli
CNR-IFAC
Via Madonna del Piano 10, 5019 Sesto Fiorentino (Italy)

Supporting information for this article is available on the WWW under https://doi.org/10.1002/cctc.202300647

and develop efficient BP-based photocatalysts for hydrogen evolution reaction (HER).[14,15] For instance, once BP is coupled with its red allotrope, affords a hetero-phase junction with a Z-scheme,[13] where the two semiconductors have the same chemical composition but different crystal lattices which promote charge separation achieving an H_2 production rate of 0.33 mmol/g·h, without using any sacrificial agent.[16] However, pristine BP suffers of rapid charge recombination,[12] thus it is necessary to combine it with a suitable wide band gap semiconductor. Noteworthy, the beneficial role of BP NS or BP quantum dots[17] once added in a small amount to photoactive semiconductors as *g*-C_3N_4,[18,19,20] TiO_2,[21,22] $BiVO_4$,[23] CdS[24,25,26] or covalently linked to MoS_2[27] was shown. In the present work, we have constructed a ternary heterostructure where the main component is commercial TiO_2 (P25), a *n*-type semiconductor having a wide band gap (~3.2 eV) which has been integrated with in-house produced BP. The latter is a *p*-type semiconductor thus it is expected the formation of p-n heterojunction between TiO_2 and BP which is beneficial for the charge separation by forming an inner electrical field between the two semiconductors.[28] CoP NPs have been added as a co-catalyst being well known the high catalytic activity of cobalt and cobalt phosphide[29] in HER, once coupled with BP[30] or with TiO_2.[31] The advantages of this nanocomposite are manifold, first of all it shows a remarkable H_2 production rate without using noble metal in comparison to known TiO_2/BP hybrids where Pt(0) photodeposition has been necessarily carried out to promote the HER,[32,33] see Table S4. Additionally, our photocatalyst can be easily prepared by sonicating a suspension of the three components, thus it can be very easily scaled up. After a fine tuning of the weight percentage of BP and of the co-catalyst CoP, the best ternary composite resulted TiO_2/BP(1%)/CoP(2%), affording a hydrogen evolution rate of 7.40 mmol/g·h, which is respectively 9 and 37 times higher in comparison to TiO_2/BP(1%) and bare TiO_2, revealing that a synergistic effect is operative among the three components.

Results and Discussion

Morphology, structure, and optical properties

The synthetic pathway followed to prepare the ternary nanohybrid is shown in Scheme 1. BP nanosheets, see Figure S1, were fabricated by liquid phase exfoliation using as solvent dimethylsulfoxide under the action of ultrasounds.[34] CoP was synthetized in a quartz oven by a slightly modified literature procedure, and it was chosen as co-catalyst being known as highly active electrocatalyst for hydrogen evolution because it remarkably decreases the reduction potential of water.[35] Tian *et al.*[30] reported that amorphous CoP grown on BP can enhance the HER better than Pt NPs. As main component of the ternary nanohybrid TiO_2 nanoparticles (commercial P25) were selected. Measures of Zeta potential showed that TiO_2 NPs have Z = 17.9 mV, meanwhile BP NS have Z = −37.4 mV, meaning the two semiconductors can be self-assembled via electrostatic interactions. After adding CoP NPs to the suspension of TiO_2 and BP, the ternary composite was prepared by ultrasonication for six hours.

The crystallinity and phase composition of the resulting ternary nanocomposite were studied and compared with the single component using X-ray diffraction (XRD) in the range $2\theta = 10°–90°$. Figure 1 shows the patterns of BP, CoP, TiO_2/BP/CoP and of TiO_2 as a reference. The diffraction peaks of the tetragonal anatase phase (Ti_4O_8) corresponding to TiO_2 appeared at $2\theta = 25.3°$ (011), 37.7° (004), 48.0° (020), 62.7° (024), and 75.0° (125).[36] The diffraction peaks of rutile (Ti_2O_4) are much less intense (being around 20 wt%) were observed at $2\theta = 27.4°$ (110), 36.1° (011), 41.2° (111), 44.1° (120), 54.3° (121), 69.0° (031), and 69.8° (112)[37] in agreement with literature.[38] The pattern of pristine BP showed five characteristic diffraction peaks at 17.2°, 26.9°, 34.7°, 36.7° and 52.5° which correspond to the planes (020), (021), (040), (111) and (060) indexed as highly crystalline BP.[39] The diffraction peaks found at 32.0°, 35.3°, 36.7°, 46.2°, 48.4°, 52.3°, 56.4°, and 56.8° correspond to the crystal planes (002), (200), (102), (112), (202), (103), (212) and (301) of pure orthorhombic CoP phase.[40] For the ternary TiO_2/BP/CoP nanocomposite, the peaks corresponding to TiO_2 were observed while being BP only 1% wt, the relative peaks appear with very low intensity. Similarly, being CoP NPs in a very low concentration and due to their broad signals, the corresponding peaks could not be observed.

Raman spectroscopy was used to investigate the TiO_2 and BP vibrational modes upon the formation of the composites. The incident power for the Raman experiments was set as low as 0.7 mW in order not to induce any optothermal degradation of the material and it was high enough to collect spectra with a suitable signal-to-noise ratio.[41] Figure 2 shows Raman spectra

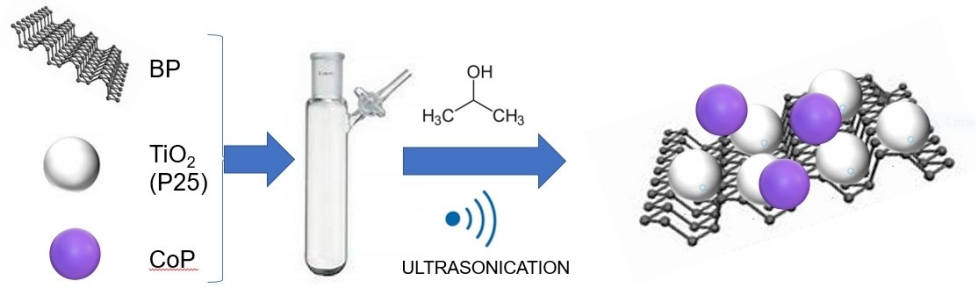

Scheme 1. Fabrication procedure of the ternary composite TiO_2/BP/CoP.

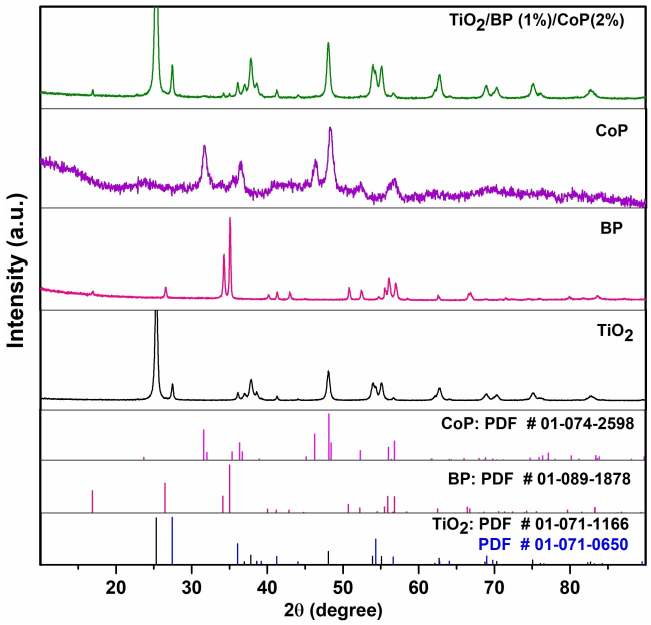

Figure 1. Powder X-ray diffraction of the single components TiO_2, BP, CoP and of the ternary composite TiO_2/BP/CoP. The minor component (20%) of TiO_2 is rutile and its peaks are shown in blue in the bottom track.

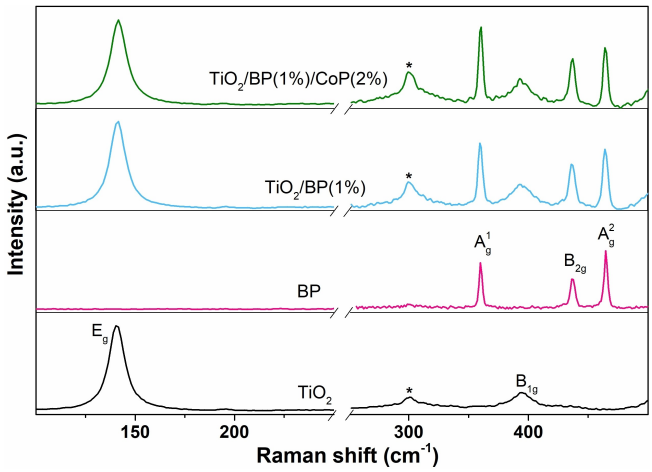

Figure 2. Raman Spectra of TiO_2, BP, TiO_2/BP(1%) and TiO_2/BP(1%)/CoP(2%) drop-casted on Si wafer. The asterisk indicates the peak of the silicon wafer used as a substrate for the deposition of the samples.

of TiO_2, BP, TiO_2/BP(1%) and TiO_2/BP(1%)/CoP(2%). In pure TiO_2, two characteristic Raman active modes with symmetries E_{1g} and B_{1g} were observed at 141 cm^{-1} and 394 cm^{-1} that were associated to anatase: the strongest peak located at 141 cm^{-1} correlates to the E_{1g} mode of O–Ti–O bond vibrations, while the peak at $\nu = 394$ cm^{-1} can be attributed to the B_{1g} phonon mode of O–Ti–O anti-symmetric bending vibrations.[42,43] For pure BP, three Raman modes were identified at 360 cm^{-1}, 436 cm^{-1}, and 464 cm^{-1} corresponding to the out-of-plane A_g^1 and in-plane B_{2g}, and A_g^2 phonon modes of orthorhombic BP.[44,45] The binary and ternary composites exhibited the characteristic Raman peaks of TiO_2 and BP described above, with no significant variation in the peak position. However, a variation in the intensity ratio of A_g^1 peak versus A_g^2 peak I_{A1g}/I_{A2g} was observed in both binary and ternary composites with respect to pure BP. The I_{A1g}/I_{A2g} value typically marks the oxidation degree of the BP nanosheets as a value of >0.2 indicates low oxidation levels.[46] We calculated I_{A1g}/I_{A2g} value in pristine BP, TiO_2/BP(1%) and TiO_2/BP(1%)/CoP(2%) composite and resulted equal to 0.8, 1.2 and 1.5 respectively (see Table S1), suggesting a lower oxidation level of BP in the composites respect to pristine BP, since TiO_2 and CoP NPs cover the surface of the nanosheets and thus prevent a direct contact with air and moisture. Moreover, it is known that for 2D nanocrystals the intensity change of Raman mode is commonly related to an electron transfer behavior.[47] In our case, the increasing intensity of I_{A1g}/I_{A2g} ratio can be related to the interaction of P atoms lone pairs with O atoms of TiO_2 and Co atoms. These interactions may cause a variation of inter-plane Raman vibrations of BP in the composites and thus highlight the formation of stacking interactions in a multi-component heterostructure.[47,48]

TEM inspection shows BP flakes decorated by TiO_2 NPs having average size between 10 and 20 nm and CoP NPs, see Figure 3a. The HAADF and EDX data (Figure 3b–c) show that phosphorene, anatase and CoP are assembled together forming an heterostructure. To further confirm the presence of all the three components, the HRTEM images were recorded on the portion that, according to HAADF and EDX data contain the required component. The analysis of a titania containing region showed the presence of the 0.35 nm lattice fringe that is ascribed to the (101) planes of anatase (Figure 3d).[49] The HRTEM analysis of the phosphorene containing region (Figure 3e) showed the occurrence of the (112) lattice fringe characteristic of phosphorene at 0.18 nm. This spacing is in good agreement with what previously observed in the literature.[50] The presence of CoP NPs was confirmed by the occurrence of the CoP (111) lattices lines at 0.25 nm, see Figure 3f.[51]

XPS measurements were carried out to obtain information on the chemical state of the elements in the binary and ternary nanocomposite. Figure 4 shows the binding energy of Ti $2p_{3/2}$ and Ti $2p_{1/2}$ in TiO_2 which is located at 458.1 eV and 463.8 eV respectively, and this is consistent with Ti^{4+} in the TiO_2 lattice.[52] After forming the p-n junction with BP NS, these two peaks exhibited shifts to higher binding energies going to 458.4 eV and 464.2 eV respectively, that means an increase of 0.3 and 0.4 eV respect to pure TiO_2. The increase in binding energy corresponds to a decrease of electron concentration in titanium, indicating the presence of a strong interaction likely due to Ti–O–P bond formation. Going to the ternary TiO_2/BP(1%)/CoP(2%) nanocomposite the increase in binding energy is slightly higher respect to TiO_2, see Figure 4, being B.E. = 458.5 eV for Ti $2p_{3/2}$ and B.E. = 464.3 eV for Ti $2p_{1/2}$.

In the core-level O1s XPS spectrum, the main peak shifts as well to higher binding energy, passing from B.E. = 529.4 eV in bare TiO_2 to B.E. = 529.8 eV in TiO_2/BP/CoP as shown in Figure S2. The minor peak at B.E. = 532.0 eV in pure TiO_2 can be ascribed to –OH functional group on the surface of TiO_2.[32] The XPS core-level P 2p spectra are summarized in Figure 5, where it is shown for BP a deconvolution in two peaks at B.E. = 129.5

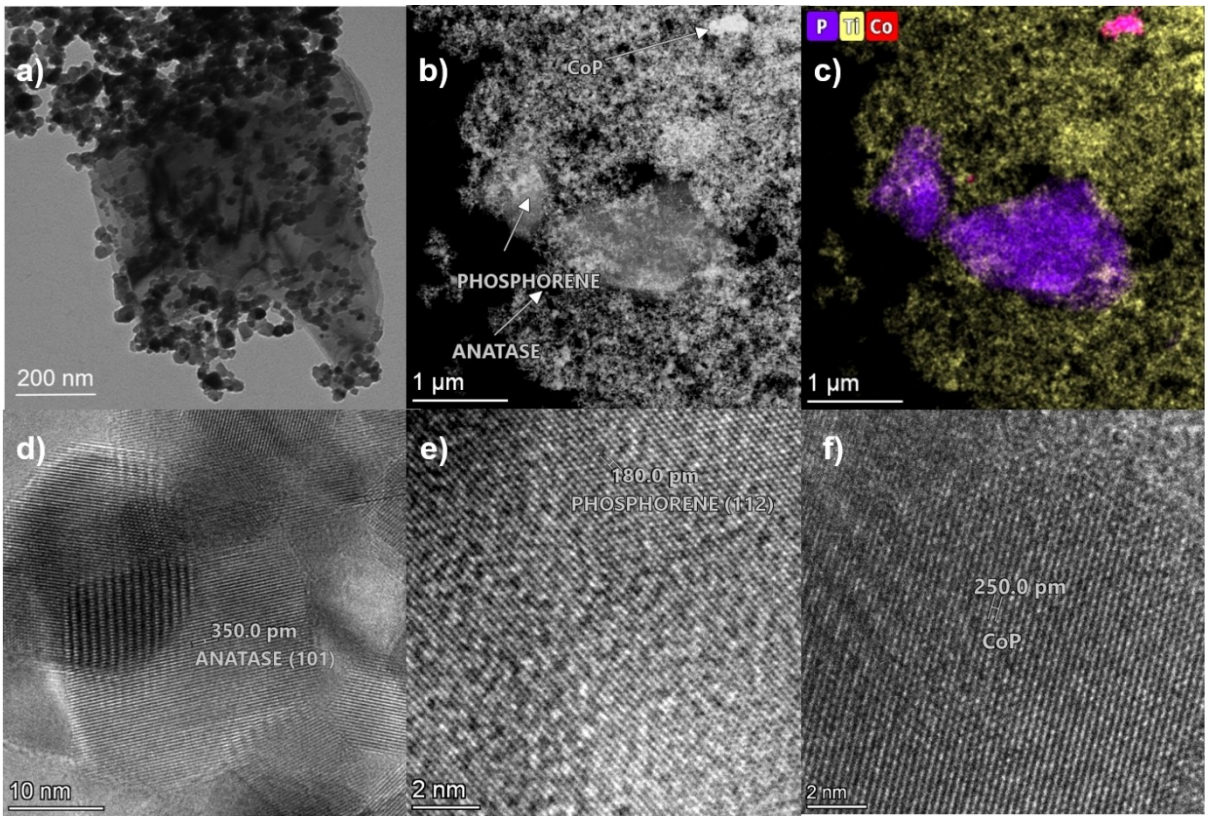

Figure 3. a) Bright field TEM image and b) HAADF image of TiO_2/BP(1 %)/CoP(2 %), c) the corresponding EDX map of the P, Ti and Co X-ray K-emissions; d) HRTEM of the region with anatase; e) HRTEM of the region with phosphorene; f) HRTEM of the region with cobalt phosphide.

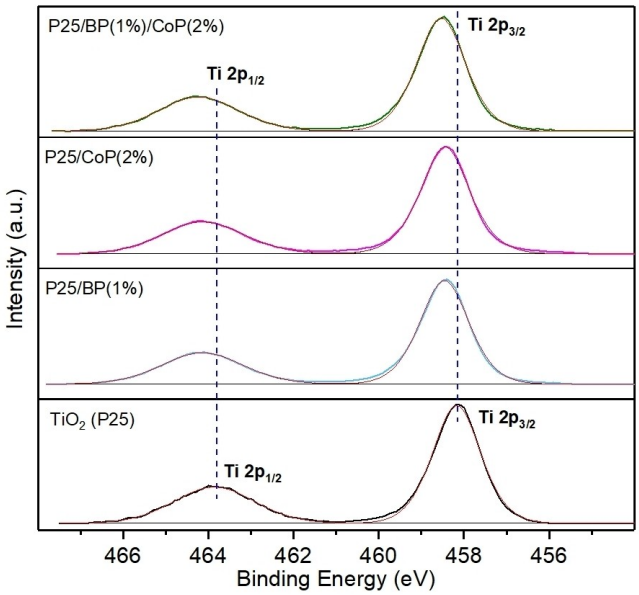

Figure 4. Core level Ti 2p XPS spectra of TiO_2, TiO_2/BP(1 %), TiO_2/CoP(2 %) and TiO_2/BP(1 %)/CoP(2 %).

and 130.4 eV, assigned respectively to P $2p_{3/2}$ and P $2p_{1/2}$ which characterize elemental phosphorus.[53] In the case of CoP, see Figure 5a, we have similarly a deconvolution in two peaks at 129.2 and 130.1 eV, slightly shifted to minor binding energy in comparison to elemental P due to their phosphide nature,[54] additionally two peaks are observed at 133.7 and 134.6 eV, due to inevitably superficial oxidation. In the ternary composite, we find the doublet assigned to P–P bonds at B.E. = 129.3 eV and B.E. = 130.1 eV, arising from the presence of BP and CoP in the composite; the main peak at B.E. = 133.5 eV characteristic of P–O bonds, see Figure 5c, can be attributed to the formation of Ti–O–P bonds in agreement with what observed above for Ti and due as well to superficial oxidation of BP that gives oxides of general formula P_xO_y[55] and to the eventual oxidation of CoP.[56] The XPS core level Co 2p spectrum (Figure S3) for CoP presents a peak at 778.4 eV, slightly shifted to higher binding energy respect to metallic Co,[56] while a second peak at 782.0 eV suggests the presence of Co–O bonds deriving from a mere superficial oxidation.[57] In the ternary composite, we could not find any signal due to cobalt owing to its very low amount (2 wt %).

Photocatalytic H_2 production activity

The light-driven hydrogen production of the synthetized heterostructures was examined under UV-Vis irradiation using methanol as sacrificial hole scavenger in aqueous solution. Pure TiO_2 exhibited the lowest H_2 production, 200 μmol/g·h as shown in Figure 6a. Thus, we loaded TiO_2 with a varying amount of BP in the range 0.5–2.0 wt.% and the maximum hydrogen evolution rate of 830 μmol/g·h (with an estimated

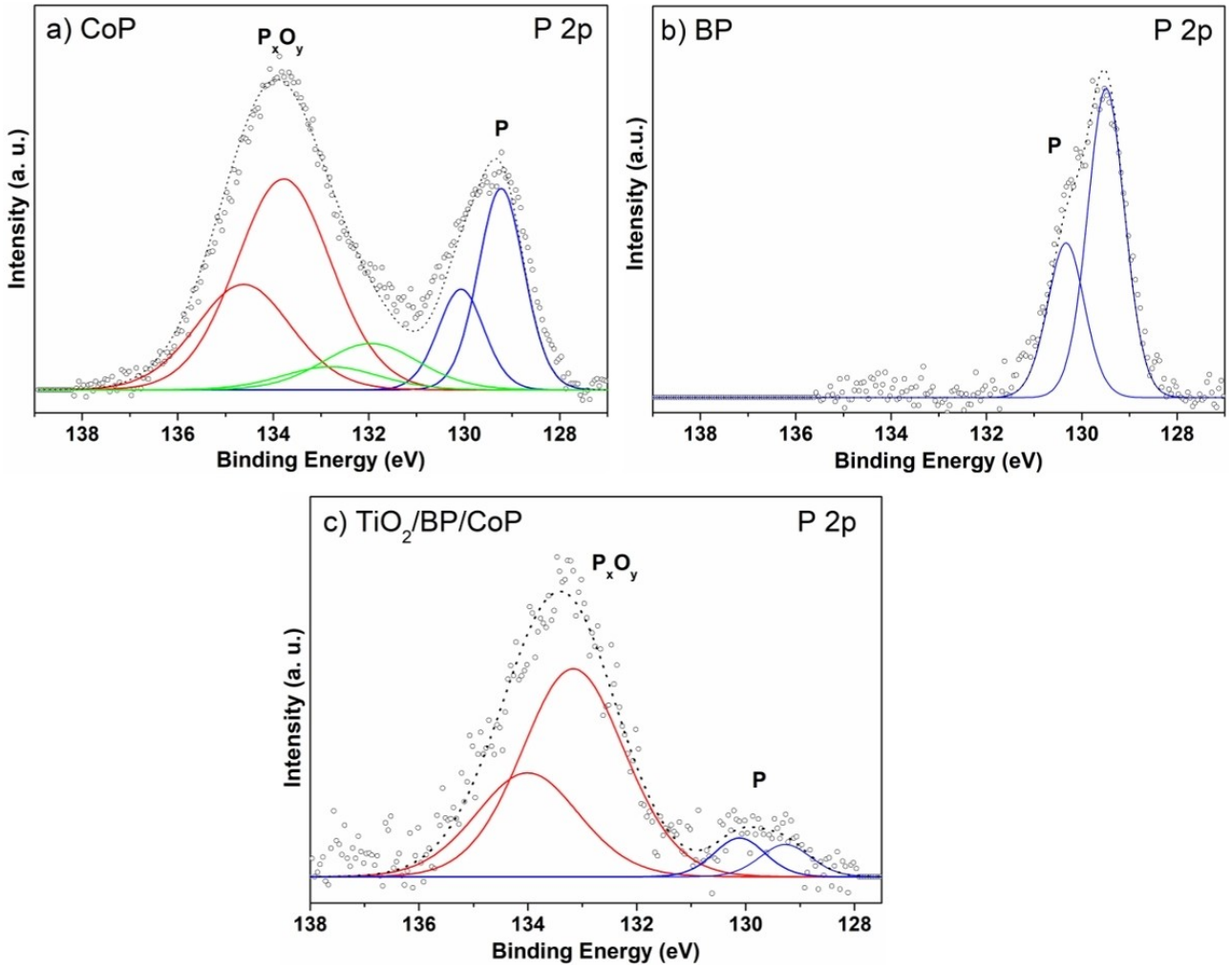

Figure 5. XPS P 2p core level spectra of a) CoP, b) pristine BP, and c) TiO_2/BP(1%)/CoP(2%).

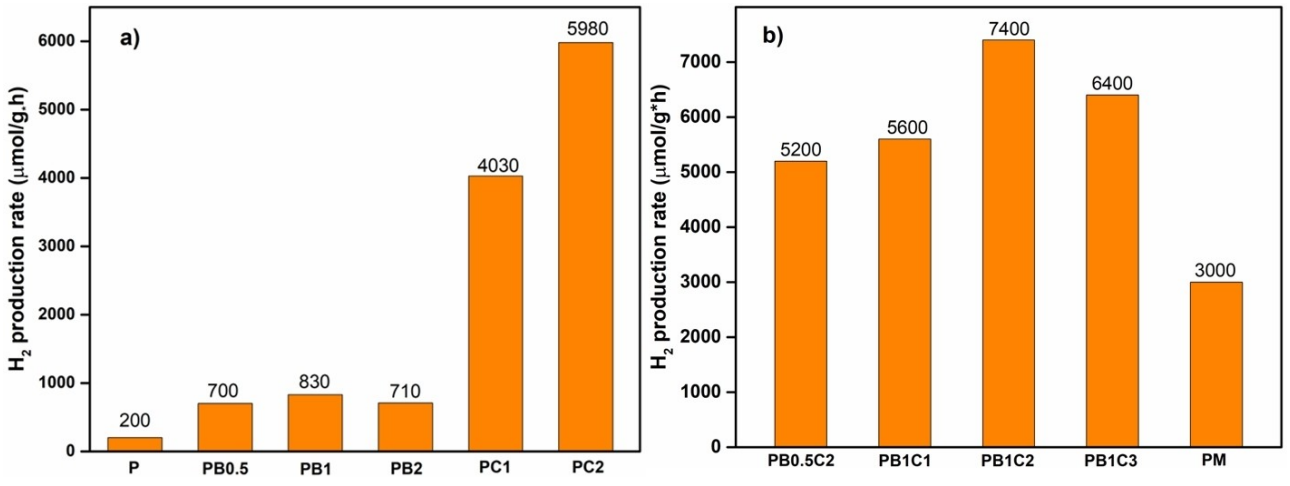

Figure 6. Photocatalytic H_2 production during five hours of (a) pure TiO_2 and binary composites TiO_2/BP, TiO_2/CoP and of (b) ternary composites and physical mixture (PM) of the three components. Legend: P = TiO_2 (P25), B = BP, C = CoP, the numbers represent the weight % of each component.

error of ±9 μmol/g·h) was observed for BP equal to 1% wt, resulting 4 times higher than pure TiO_2, see Figure 6a. When the amount of BP is increased to 2% wt, the photocatalytic activity decreases, which is likely due to a shielding effect being the surface of TiO_2 covered by a larger amount of BP.[28] On the opposite, once the BP loading diminished to 0.5 wt%, the

formed heterojunction with TiO_2 is correspondingly reduced, resulting in a decreased activity. The heterojunction TiO_2/BP has been studied recently[17] though using BP quantum dots instead of nanosheets, and an hydrogen production of 112 μmol/g·h was afforded that reached a value of 286 μmol/g·h after adding 1 wt.% of Pt NPs. Noteworthy, in our case once CoP nanoparticles were loaded on TiO_2/BP, the H_2-production of the ternary TiO_2/BP/CoP heterostructure was remarkably increased, and it was found out that the best combination is for a loading of 1 wt.% BP and 2 wt.% CoP as shown in Figure 6b. The ternary composite TiO_2/BP(1%)/CoP(2%) exhibits the highest photocatalytic H_2-production rate of 7400 μmol/g·h (with an estimated error of ±65 μmol/g·h) which is respectively 9 and 37 times higher in comparison to TiO_2/BP(1%) and bare TiO_2.

A further test was carried out, by using as catalyst a physical mixture TiO_2 + BP + CoP (PM) in the same proportion as the best performing ternary PB1 C2, which gave a hydrogen production rate of 3.0 mmol/g·h, that is 2.5 times lower than the ternary obtained by ultrasonication, as shown in Figure 6b. This confirmed the presence of a chemical interaction Ti–O–P as outlined by XPS, that provides at atomic level a charge transfer channel which enhances the electron transfer from BP to TiO_2 and consequently to CoP. The influence of different hole scavengers as methanol, triethanolamine, lactic acid and glycerol was tested in the reaction rate. Methanol resulted the best one, affording the highest hydrogen evolution rate of 7.4 mmol/g·h, see Figure S5.

Finally, the cycle stability of the ternary TiO_2/BP/CoP was tested and resulted robust and highly reproducible after three reaction cycles as shown in Figure S6. The solid catalyst was recovered at the end of the cycling tests and it was analyzed by PXRD which confirmed that the structural integrity was maintained unaltered, see Figure S7. The morphology of the photocatalyst was checked by SEM imaging coupled with EDX elemental analysis and as shown in Figure S8, the heterostructure based on BP nanosheets covered by TiO_2 and CoP NPs was preserved, demonstrating such integration of BP effectively improves its stability even under long-term irradiation in water.

Electrochemical properties and charge transfer dynamics

To unravel the origin of the remarkable hydrogen evolution rate and photo-stability of the TiO_2/BP/CoP nanostructures, the light harvesting capacity, photo charge carriers separation and migration were exhaustively characterized by UV–Vis diffusion reflectance spectrometry (DSR), photoluminescence (PL) and electrochemical impedance spectroscopy (EIS). Firstly, the light harvesting capability of BP, TiO_2, and TiO_2/BP nanostructures were measured by DSR, see Figure 7a. BP nanosheets show a

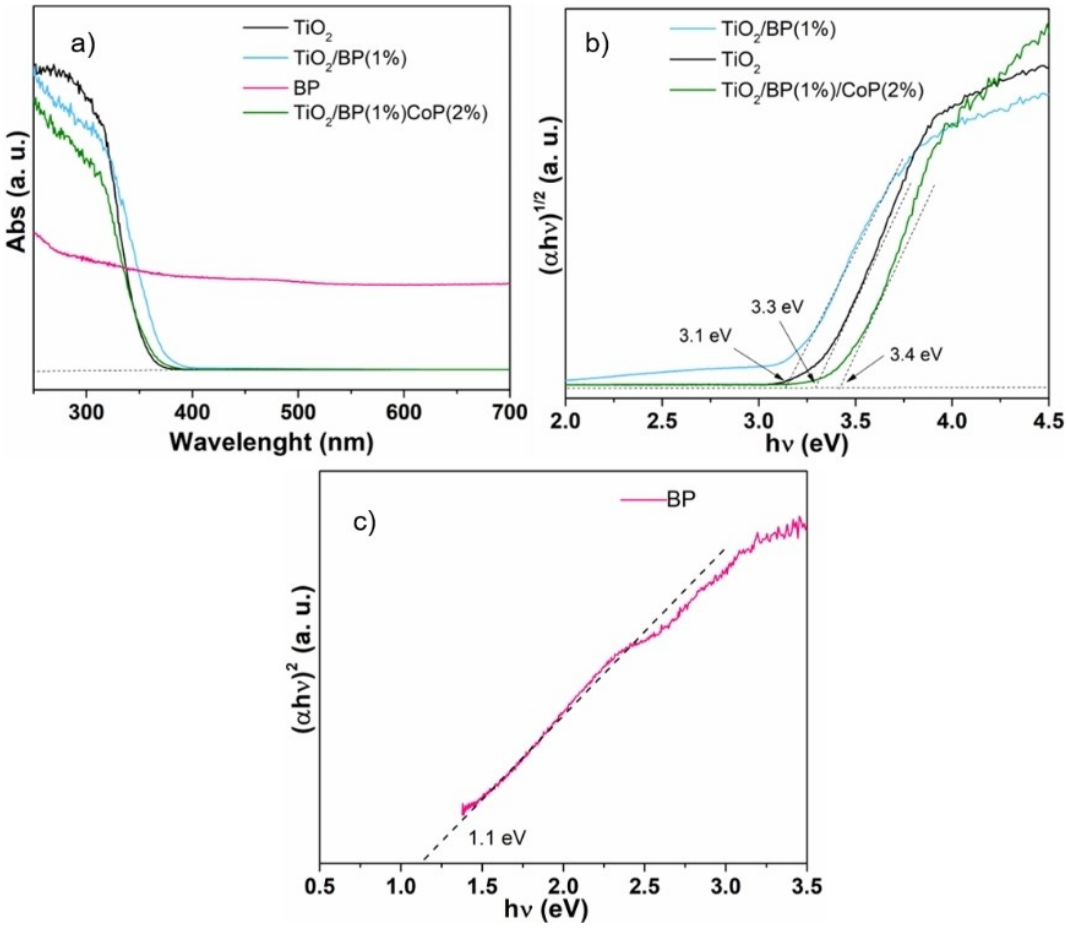

Figure 7. a) UV-Vis DRS of the prepared samples with the reference TiO_2, b) Tauc plots of TiO_2, TiO_2/BP(1%) and TiO_2/BP(1%)CoP(2%); c) Tauc plot of BP.

very wide absorption ranging from UV to NIR region, while the absorption region of pure TiO_2 is the ultraviolet region ($\lambda < 360$ nm). After loading TiO_2 with 1% wt of BP, it can be observed a red shift of the spectrum that confirms a strong interfacial interaction between TiO_2 and BP as already observed by XPS. The optical band gap energies (E_g) were estimated by Kubelka-Munk function according to the formula $\alpha h\nu = A(h\nu - E_g)^{n/2}$ where α is the absorption coefficient, $h\nu$ is the incident photon energy, A is a constant and the n value is determined by the type of optical transition of the semiconductor. Being TiO_2 an indirect semiconductor,[58] than it is taken $n = 1/2$ for TiO_2-based nanocomposites, meanwhile BP is known as a direct semiconductor[59] thus $n = 2$. The corresponding Tauc plots are shown in Figure 7b and 7c where extrapolating the linear region of the Kubelka-Munk function to the photon energy, it is obtained the value of E_g. It is observed a reduction of the bandgap passing from pure TiO_2 ($E_g = 3.3$ eV) to the binary TiO_2/BP ($E_g = 3.1$ eV), that ensures an increased light absorption in the visible region and accelerates the electron transfer, being lower the energy gap from the valence to the conduction band.

To calculate the conduction band (CB) and valence band (VB) energy levels of BP NS, TiO_2 and the ternary composite, electrochemical impedance measurements were carried out and the corresponding Mott-Schottky plots are shown in Figure 8. From the extrapolation of the linear region of the Mott-Schottky plot to the *x*-axis, the flat-band potential V_{fb} is obtained and correcting for the standard potential of the Ag/AgCl electrode, V_{fb} of pristine BP, TiO_2, TiO_2/BP and ternary hybrid was calculated to be −0.25, −0.08, −0.20 and −0.54 *vs.* NHE (normal hydrogen electrode), respectively. The flat-band potential can be approximate as *quasi Fermi level* and lies 0.1 V lower the conduction band minimum (CBM).[60] Thus, the E_{CB} was estimated to be −0.35 V for BP, −0.18 V for TiO_2, −0.30 V for TiO_2/BP and −0.64 V for the ternary hybrid (Figure 8).

The progressive negative shift of the flat band potential going from pure TiO_2 to TiO_2/BP and finally to the ternary hybrid, implies that the latter has the largest carried density N_D, as it can be calculated from the slope of the linear portion of the Mott-Schottky graph using equation 1:

$$\frac{1}{C^2} = \frac{2}{\varepsilon \cdot \varepsilon_0 \cdot e_0 \cdot A^2 \cdot N_D}\left(E - E_{FB} - \frac{kT}{e_0}\right) \quad (1)$$

Intriguingly, for the ternary composite the calculated value for N_D was 9.64×10^{20} cm^{-3} meanwhile for pure TiO_2 was $N_D = 6.83 \times 10^{20}$ cm^{-3}, revealing an increase of 29% of carrier density N_D upon functionalization with BP and CoP, see Table S3. As a consequence, the conductivity of the photocatalyst is increased and is promoted the separation of the charge carriers at the heterojunction interface. The energy position of the valence-band could then be calculated according to the equation: $E_{VB} = E_{CB} + E_g$ where E_g is the band gap of the semiconductor. From these experimental magnitudes and taking into account that TiO_2 is n- and BP is p-type semiconductor, a type II p-n heterojunction is expected at the interface between TiO_2 and BP and consequently a photocatalytic reaction mechanism could be derived as shown in Figure 9.

BP has a more negative CB ($E_{CB} = -0.33$ V) in comparison to TiO_2 ($E_{CB} = -0.18$ V) which allows the transfer of photogenerated electrons from BP to the CB of TiO_2. CoP NPs work as co-catalyst and acceptor of electrons and offer reactive sites for proton reduction. The Fermi level[31] E_F of CoP is equal to +0.173 eV respect to NHE, as shown in Figure 9. This kind of p-n heterojunction has proven to be a successful strategy since can promote an effective spatial separation of the photo-induced electrons and holes and as a result, they have a longer lifetime and a lower recombination rate.[9,52,61] To confirm the charge separation and transfer behavior of photogenerated carriers, photoluminescence spectra (PL) and electrochemical

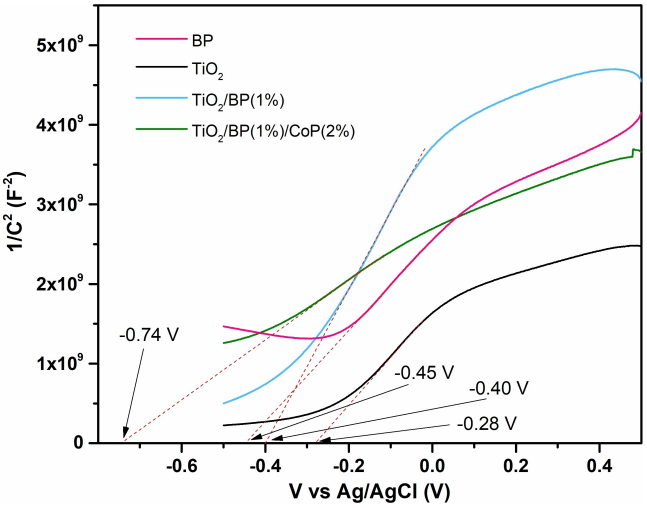

Figure 8. Mott-Schottky plots of pure TiO_2, TiO_2/BP(1%) and TiO_2/BP(1%)/CoP(2%). Dashed lines show an approximate linear fit used to estimate the V_{fb}.

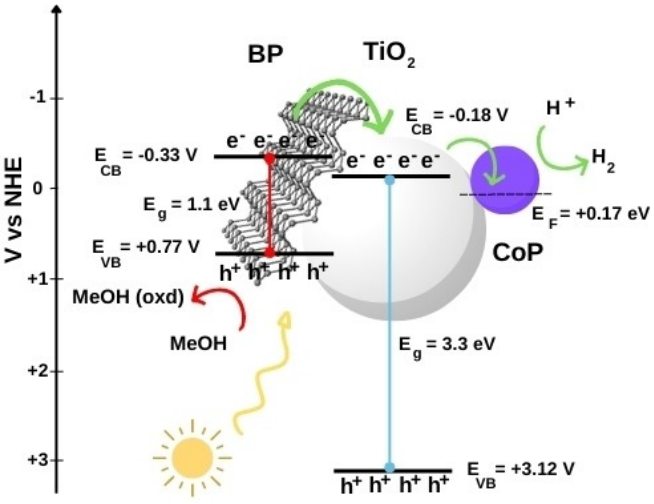

Figure 9. Band energy level diagram and the proposed photocatalytic reaction mechanism over TiO_2/BP/CoP under UV-Vis irradiation. E_F stands for Fermi level.

impedance (EIS) measurements were performed on the single components and in the binary and ternary derivatives, see Figure 10, 11 and S8. At $\lambda = 325$ nm of photoexcitation, all samples show a PL emission band centered around $\lambda = 410$ nm, which is originated from their band edge emission upon light excitation. As shown in Figure 10, pure TiO_2 exhibits the most intense emission peak, which is characteristic of the radiative recombination of its charge carriers, remarkably the highest quenched emission intensity is found for the ternary TiO_2/BP(1%)/CoP(2%) when compared with the binary TiO_2/BP and TiO_2/CoP, confirming that an efficient charge separation is achieved once BP and CoP are both loaded on TiO_2.

The interface charge mobility of TiO_2, BP, TiO_2/BP, TiO_2/CoP and TiO_2/BP/CoP nanocomposites was evaluated by EIS, where

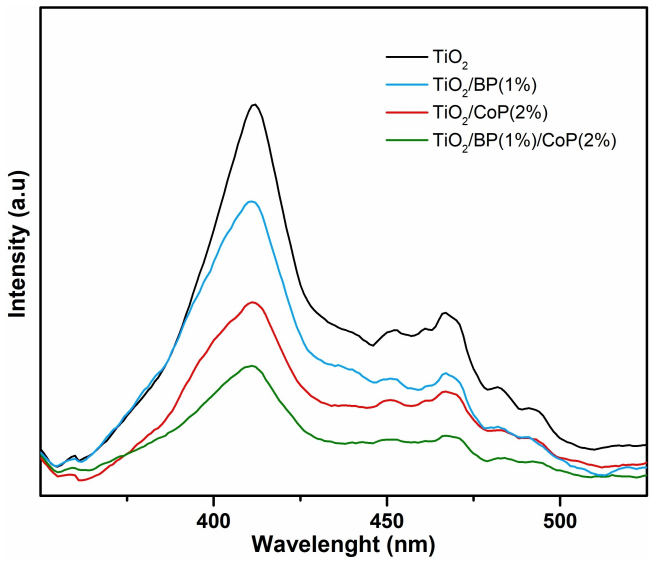

Figure 10. Photoluminescence spectra of TiO_2, TiO_2/BP(1%), TiO_2/CoP(2%) and TiO_2/BP(1%)/CoP(2%).

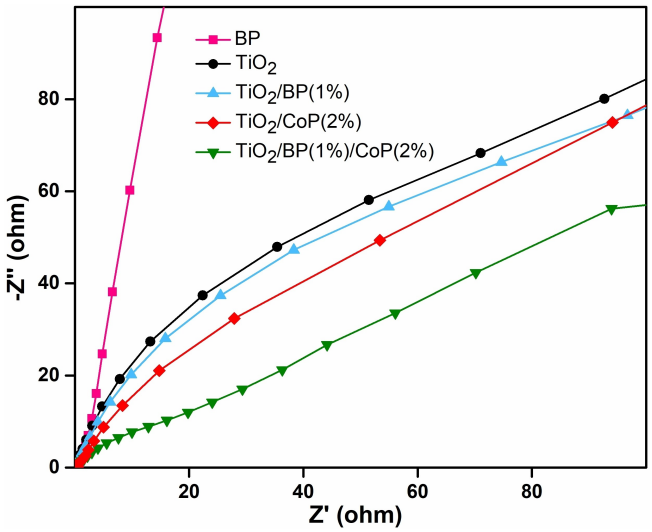

Figure 11. Nyquist plots measured under a bias potential of 0.3 V (vs. Ag/AgCl) in a 0.5 M Na_2SO_4 solution. The symbols correspond to the measured data and the lines represent the fitting results.

a small arc radius stands for an enhanced charge transfer efficiency inside the material. Noteworthy, the smallest arc radius was observed for the three-component photocatalyst TiO_2/BP/CoP in comparison to TiO_2, BP, TiO_2/BP(1%) and TiO_2/CoP(2%), see Figure 11, showing that the heterostructure resulting from the integration of BP nanoflakes with CoP NPs and TiO_2, effectively promotes the charge carrier separation and the interfacial charge transfer rate.[62]

Doing a comparison among ternary composites TiO_2/BP-(1%)/CoP(y) which differ for CoP wt% content (y = 1.0, 2.0, 3.0%), it emerges a great improvement in charge transfer passing from y = 1.0 to 2.0, which does not improve further for y = 3.0%, as shown in Figure S9.

Finally, comparing our best performing nanocomposite TiO_2/BP(1%)/CoP(2%) with known analogous TiO_2-BP catalysts, see Table S4, it emerges our ternary composite as the best photocatalyst in terms of H_2 production (mmol/g·h) which rivals with analogous TiO_2/BP systems where 3 wt% Pt has been replaced by 2 wt% CoP.

Conclusions

In this work, we have fabricated a ternary TiO_2/BP/CoP heterostructure by an easy and reproducible synthesis carried out by ultrasonication, thus it can be easily tuned the quantity of each components and scaled up. The large lateral size of BP nanosheets assures a wide interfacial contact area and behaves as a bidimensional nanoplatform where the small-sized TiO_2 and CoP NPs can be accommodated. It was shown that addition of a very low amount of BP(1%) and CoP(2%) to TiO_2, achieves the most efficient charge separation and the least internal resistance, thus speeding up the hydrogen evolution rate and reaching an excellent hydrogen production activity of 7.4 mmol/g·h, which is 37 times superior than pristine TiO_2. From the mechanistic point of view, it was proposed a mechanism where the photogenerated electrons migrate from the CB of BP to the CB of TiO_2 and finally to the CoP active sites where the proton reduction takes place. In summary, the enhanced performance can be correlated not only to the suitable band edge position but also to the synergy among the three components arising from an enhanced charge transfer as evidenced by XPS, Raman and Mott-Schottky measurements, where the carrier density N_D is greatly promoted once BP and CoP are loaded on TiO_2. Noteworthy, the ternary TiO_2/BP/CoP heterostructure provides a new class of photocatalysts stable in the recycling and opens the way to develop noble metal-free heterostructures for solar conversion and hydrogen production.

Experimental Section

Reagents

Red phosphorus (ultrahigh grade, purity ≥99.99%), Sn (purity ≥99.99%), SnI_4 (99.8%), cobalt nitrate hexahydrate (purity ≥98%), urea (purity ≥99%) and sodium hypophosphite (purity ≥99%)

were purchased from Merck. Titanium dioxide (P25, purity ≥99.5%) was received from Evonik. All chemicals were used as received.

Preparation of BP nanosheets

First, bulk black phosphorus microcrystals were synthesized according to a published procedure.[63]

Afterwards, few-layer black phosphorus nanosheets were obtained by liquid phase exfoliation of black phosphorus crystals in dimethylsulfoxide under the action of ultrasounds as previously described by some of us.[34]

Preparation of CoP nanoparticles

The procedure is a slight modification of the published protocol.[31] $Co(NO_3)_2 \cdot 6H_2O$ (292.0 mg, 1.00 mmol) was dissolved in 10 mL of distilled and degassed H_2O. Afterwards, a urea solution was added (600.1 mg, 1.00 mmol) dissolved in 10 mL of distilled and degassed H_2O and a pink solution was obtained. The latter was stirred for 30 minutes and transferred inside a Teflon-lined autoclave. The autoclave was then heated to110 °C in an oven for 24 hours. After this time the autoclave was left to cool down to RT, then it was opened and the pink powder of $Co(OH)_2$ was isolated by centrifugation. Three washing/centrifugation cycles were carried out using degassed ethanol, then the solid was dried under vacuum overnight. Powder $Co(OH)_2$ (25.0 mg, 0.270 mmol) and $NaH_2PO_2 \cdot H_2O$ (250.0 mg, 2.38 mmol) were mixed and grinded together until uniform. Then the sample was annealed at 300 °C for 2 h in a nitrogen flow at a ramp rate of 5 °C min^{-1}. Finally, the obtained black solid was collected and washed/centrifuged three times with deionized water and ethanol and dried at vacuum oven. Yield: 85%.

Preparation of TiO_2-BP binary composites

TiO_2 (99.0 mg, 1.24 mmol) and exfoliated black phosphorus (1.0 mg, 0.032 mmol) were dispersed in 80 mL of degassed 2-propanol by stirring. The resulting suspension was ultra-sonicated (170 W, 35 KHz) for 3 hours, afterwards the gray powder TiO_2/BP was isolated by centrifugation. Two washing/centrifugation cycles were carried out using degassed ethanol, then the solid was dried under vacuum overnight. For comparison, a series of TiO_2/BP(x) were obtained, where x represents the weight percentages of BP in the various composites, x = 0.5, 1.0, 2.0 wt% respectively.

Preparation of TiO_2-CoP binary composites

TiO_2 (98.0 mg, 1.23 mmol), and CoP (2.0 mg, 0.022 mmol) were dispersed in 80 mL of degassed 2-propanol. The dispersion was ultra-sonicated (170 W, 35 KHz) for 6 hours keeping the temperature of the sonication bath fixed at T = 20 °C. Afterwards the light gray powder was isolated by centrifugation. Two washing/centrifugation cycles were carried out using degassed ethanol, then the solid was dried under vacuum overnight. A series of TiO_2/CoP(y) composites were obtained, where y = 1.0, 2.0% represent the weight percentages of CoP in the composites.

Preparation of TiO_2-BP-CoP ternary composites

TiO_2 (97.0 mg, 1.21 mmol), exfoliated black phosphorus (BP, 1.0 mg, 0.032 mmol) and CoP (2.0 mg, 0.022 mmol) were dispersed in 80 mL of degassed 2-propanol. The dispersion was ultra-sonicated (170 W, 35 KHz) for 6 hours keeping the temperature of the sonication bath fixed at T = 20 °C. Afterwards the gray powder of the ternary composite TiO_2/BP/CoP was isolated by centrifugation. Two washing/centrifugation cycles were carried out using degassed ethanol, then the solid was dried under vacuum overnight. A series of TiO_2/BP(x)/CoP(y) composites were obtained, where x and y represent the weight percentages of BP and CoP in the various composites, x = 0.5, 1.0% and y = 1.0, 2.0, 3.0% respectively. The wt% composition was also confirmed by ICP analysis, see Table S2.

Preparation of TiO_2-BP-CoP physical mixture (PM)

TiO_2 (48.5 mg, 0.60 mmol), exfoliated black phosphorus (BP, 0.5 mg, 0.016 mmol, 1 wt%) and CoP NPs (1.0 mg, 0.011 mmol, 2 wt%) were individually dispersed in 4 mL of degassed 2-propanol. The three dispersions were ultra-sonicated (170 W, 35 KHz) for 30 minutes keeping the temperature of the sonication bath fixed at T = 20 °C. Afterwards they were mixed together and the resulting ternary TiO_2-BP-CoP mixture was isolated by centrifugation. Two washing/centrifugation cycles were carried out using degassed ethanol, then the solid was dried under vacuum overnight.

Characterization

X-ray diffraction (XRD). Data were collected on the powder samples with a Panalytical X'Pert PRO diffractometer (The Netherlands), operating in Bragg-Brentano parafocusing geometry with a Cu target and Kα radiation (λ = 1.5418) at 40 kV beam voltage and 40 mA current. The data were collected in the 5°–90° 2θ range, with steps of 0.01° and counting time of 130 s.

TEM microscopy. Transmission Electron Microscopy studies were carried out at Ce.ME CNR (Sesto Fiorentino, Italy) using a Philips CM12 electron microscope operating at an accelerating voltage of 80 kV. Few drops of each sample were suspended in methanol and placed on the TEM copper/carbon grid, dried under a stream of nitrogen, and measured.

SEM microscopy. Scanning Electron Microscopy experiments were carried out at Ce.ME CNR (Sesto Fiorentino, Italy) using a Dual Beam FIB/SEM (TESCAN GAIA3, Czeck Republic) ultrahigh resolution field emission microscope at 5 KeV voltage and prepared as described above for TEM analysis.

High-resolution TEM microscopy. HRTEM images were acquired using a ThermoFisher Talos F200X G2 at an accelerating voltage of 200 kV and a camera resolution of 4096×4096 pixels without a lens aperture. High Angle Annular Dark Field images were acquired with an annular STEM detector using a convergent beam with an angle of 10.5 mrad. EDX maps were taken with a Super X spectrometer equipped with four 30 mm^2 silicon drift detectors for a collection angle of 0.7 srad.

XPS. X-ray Photoelectron Spectroscopy (XPS) measurements were performed at the Chemistry Department, University of Florence (Italy) in an ultra-high vacuum (10^{-9} mbar) system equipped with a VSW HAC 5000 hemispherical electron energy analyzer and a non-monochromatized Mg–Kα X-ray source (1253.6 eV). The source power used was 100 W (10 kV×10 mA) and the spectra were acquired in the constant-pass-energy mode at E_{pas} = 44 eV. The overall energy resolution was 1.2 eV as a full-width at half maximum (FWHM) for the Ag $3d_{5/2}$ line of a pure silver reference. The recorded spectra were fitted using XPS Peak 4.1 software employing Gauss-Lorentz curves after subtraction of a Shirley-type background. The samples were dropcasted from a suspension in methanol, dried under a stream of nitrogen and introduced in the UHV system via a load lock under inert gas (N_2) flux, in order to minimize the exposure to air contaminants and kept in the

introduction chamber for at least 12 hours before the measurements.

UV-Vis DRS. The UV-Vis absorption and diffuse reflectance spectra were measured on the solid samples with a Shimadzu UV-2600 spectrometer using an integrating sphere with $BaSO_4$ as a reference material. By using the Kubelka-Munk equation, Tauc plots were obtained and the optical band-gap energy of the samples was extrapolated.

Raman. Raman characterization of the samples was performed at room temperature in a backscattering configuration using a LabRam HR 800EVO Raman spectrometer (Horiba France SAS) equipped with an Olympus BXFM microscope (objective X100, NA 0.9), TE cooled CCD detector (Syncerity OE), 633 nm HeNe laser and 600 grooves/mm diffraction grating. The spectral resolution was 0.9–1.8 cm^{-1}. The sample was drop-casted on silicon wafers as the substrate then it was dried in nitrogen atmosphere. The laser power at the sample was 0.7 mW and the acquisition time was 1 s. Ten to twenty spectra were registered for each sample at different locations to verify sample homogeneity and the absence of photoinduced phenomena. The reference spectrum of Si was measured contextually in each sample. Raman spectra were corrected for the baseline and Raman peak analysis was performed through the Lorentzian fitting function to calculate position, intensity and area of the characteristic peaks.

Photocatalytic H_2 production

The photocatalytic hydrogen evolution experiments were performed in a 30 mL cylindrical quartz reactor at ambient temperature ($T = 25\,°C$). 1.8 mg of catalyst was ultrasonically dispersed in 5 mL of degassed MilliQ water solution containing the desired amount of methanol (V_{H2O}: $V_{MeOH} = 4$) and the reactor was closed with a rubber cap equipped with a silicone septum. A 300 Watt Xenon arc lamp (mKs-Newport, USA) equipped with a band cut-off filter ($\lambda \leq 780$ nm) was used as the light source. The stirring was started when the light was irradiated on the sample. The measurements were carried out irradiating in the UV-Vis region at a light intensity of 1.4 sun (140 mW/cm^2) which was calibrated using a Si reference cell. Before irradiation, nitrogen gas was bubbled for 30 min to remove the air inside. The evolved hydrogen gas was sampled every hour and determined using an off-line gas chromatograph (Shimadzu GC-2010, Japan) equipped with thermal conductivity detector (TCD) and a 5 Å molecular sieve column.

Electrochemical measurements

Electrochemical measurements including electrochemical impedance spectra (EIS) and specific capacitance performances (cyclic voltammetry, CV) were carried out in a standard three electrode cell on an electrochemical workstation (PARSTAT 2273 potentiostat). The EIS (perturbation voltage 20 mV, frequency 110 KHz–100 mHz) and CV were measured using an Ag/AgCl electrode as the reference electrode, a platinum plate as the counter electrode and 0.5 M Na_2SO_4 aqueous solution as the electrolyte. To prepare the working electrode, the as-synthesized BP, TiO_2/BP and TiO_2/BP/CoP nanocomposites were first dispersed in MeOH (1.0 mL). The dispersion containing the catalyst (3.0 mg/mL) was deposited by drop-coating on a fluorine-doped tin oxide (FTO) conductive glass substrate (2.0 cm^2) and was dried under a stream of nitrogen before measurements. Mott-Schottky (M-S) curves were measured under an arc amplitude of 10 mV and frequency of 1 kHz.

Photoluminescence

PL measurements were registered using a Jasco spectrofluorometer model FP-8300. The powder samples TiO_2, TiO_2/BP(1%), TiO_2/CoP(2%) and TiO_2/BP(1%)/CoP(y%) were analyzed by irradiating at a wavelength close to the maximum absorption in the corresponding UV-Vis spectrum, i.e. $\lambda = 325$ nm.

Supporting Information

Additional references cited within the Supporting Information.[64–69]

Acknowledgements

M. C. and M. S. R. acknowledge the project "FERMAT – Fast ElectRon dynamics in novel hybrid organic-2D MATerials" funded by the MUR Progetti di Ricerca di Rilevante Interesse Nazionale (PRIN) Bando 2017 – Grant number 2017KFY7XF. Dr. Andrea Ienco (CNR ICCOM) is gratefully acknowledged for running powder X-ray spectra. The authors thank Mr. Carlo Bartoli (CNR ICCOM) for his unvaluable help and technical assistance in the set-up of photocatalytic equipment and for constructing the Teflon-lined autoclave used for the hydrothermal synthesis.

Conflict of Interests

The authors declare no conflict of interest.

Data Availability Statement

The data that support the findings of this study are available in the supplementary material of this article.

Keywords: Black Phosphorus · Cobalt Phosphide · Hydrogen Evolution · Photocatalysis · Titania

[1] R. Bhandari, R. R. Shah, *Renewable Energy* **2021**, *177*, 915–931.
[2] I. Staffell, D. Scamman, A. Velazquez Abad, P. Balcombe, P. E. Dodds, P. Ekins, N. Shahd, K. R. Ward, *Energy Environ. Sci.* **2019**, *12*, 463–491.
[3] K. Li, B. Peng, T. Peng *ACS Catal.* **2016**, *6*, 7485–7527.
[4] M. Shabir, M. Yasin, M. Hussain, I. Shafiq, P. Akhter, A.-S. Nizami, B.-H. Jeon, Y.-K. Park, *J. Ind. Eng. Chem.* **2022**, *112*, 1–19.
[5] A. Fujishima, K. Honda, *Nature* **1972**, *238*, 37–38.
[6] A. Meng, L. Zhang, B. Cheng, J. Yu, *Adv. Mater.* **2019**, *31*, 1807660–18007691.
[7] B. Meena, M. Kumar, S. Gupta, L. Sinha, P. Subramanyam, C. Subrahmanyam, *Sustain. Energy Technol. Assess.* **2022**, *49*, 101775–101785.
[8] Q. Tan, K. Li, Q. Li, Y. Ding, J. Fan, Z. Xu, K. Lv, *Mater. Today Chem.* **2022**, *26*, 101114–101122.
[9] P. S. Basavarajappa, S. B. Patil, N. Ganganagappa, K. Raghava Reddy, A. V. Raghu, C. Venkata Reddy, *Int. J. Hydrogen Energy* **2020**, *45*, 7764–7778.
[10] S. A. Ansari, M. H. Cho, *Sci. Rep.* **2016**, *6*, 25405–25414.
[11] S. Li, Y. Hau Ng, R. Zhuc, S. Lv, C. Wu, Y. Liu, L. Jing, J. Deng, H. Dai, *Appl. Catal. B* **2021**, *297*, 120412–120419.

[12] P. Li, J. Lu, H. Cui, S. Ruan, Y.-J. Zeng, *Mater Adv* **2021**, *2*, 2483–2509.
[13] X. Zhu, T. Zhang, Z. Sun, H. Chen, J. Guan, X. Chen, H. Ji, P. Du, S. Yang, *Adv. Mater.* **2017**, *29*, 1605776–1605782.
[14] P. Vishnoi, U. Gupta, R. Pandey, C. N. R. Rao, *J. Mater. Chem. A.* **2019**, *7*, 6631–6637.
[15] P. Vishnoi, A. Saraswat, C. N. R. Rao, *J. Mater. Chem. A.* **2022**, *10*, 19534–19551.
[16] F. Liu, R. Shi, Z. Wang, Y. Weng, C.-M. Che, Y. Chen, *Angew. Chem.* **2019**, *131*, 11917–11921 and references therein.
[17] R. Guan, L. Wang, D. Wang, K. Li, H. Tan, Y. Chen, X. Cheng, Z. Zhao, Q. Shang, Z. Sun, *Chem. Eng. J.* **2022**, *435*, 135138–135146.
[18] M. Zhu, S. Kim, L. Mao, M. Fujitsuka, J. Zhang, X. Wang, T. Majima, *J. Am. Chem. Soc.* **2017**, *139*, 13234–13242.
[19] R. Boppella, W. Yang, J. Tan, H.-C. Kwon, J. Park, J. Moon, *Appl. Catal. B* **2019**, *242*, 422–430.
[20] M. Wen, J. Wang, R. Tong, D. Liu, H. Huang, Y. Yu, Z.-K. Zhou, P. K. Chu, X.-F. Yu, *Adv. Sci.* **2019**, *6*, 1801321–1801327.
[21] H. U. Lee, S. C. lee, J. Won, B.-C. Son, S. Choi, Y. Kim, S. Y. Park, H.-S. Kim, Y.-C. Lee, J. Lee, *Sci. Rep.* **2015**, *5*, 8691–8696.
[22] O. Elbanna, M. Zhu, M. Fujitsuka, T. Majima, *ACS Catal.* **2019**, *9*, 3618–3626.
[23] Z. Mingshan, F. Mamoru, M. Tetsuro, S. Zhichao, *Angew. Chem. Int. Ed.* **2018**, *57*, 2160–2164.
[24] J. Ran, B. Zhu, S.-Z. Qiao, *Angew. Chem. Int. Ed.* **2017**, *56*, 10373–10377.
[25] L. Mao, X. Cai, S. Yang, K. Han, J. Zhang, *Appl. Catal. B* **2019**, *242*, 441–448.
[26] D. A. Reddy, E. H. Kim, M. Gopannagari, Y. Kim, D. P. Kumar, T. K. Kim, *Appl. Catal. B* **2019**, *241*, 491–498.
[27] P. Vishnoi, K. Pramoda, U. Gupta, M. Chletri, R. G. Balakrishna, C. N. R. Rao, *ACS Appl. Mater. Interfaces* **2019**, *11*, 27780–27787.
[28] H. Wang, L. Zhang, Z. Chen, J. Hu, S. Li, Z. Wang, J. Liu, X. Wang, *Chem. Soc. Rev.* **2014**, *43*, 5234–5244.
[29] X. Cao, Y. Tan, H. Zheng, J. Hu, X. Chen, Z. Chen, *Phys. Chem. Chem. Phys.* **2022**, *24*, 4644–4652.
[30] B. Tian, B. Tian, B. Smith, M. C. Scott, R. Hua, Q. Lei, Y. Tian, *Nat. Commun.* **2018**, *9*, 1397–1407.
[31] Q. Liu, J. Huang, H. Tang, X. Yu, J. Shen, *J. Mater. Sci. Technol.* **2020**, *56*, 196–205.
[32] J. Wu, S. Huang, Z. Jin, J. Chen, L. Hu, Y. Long, J. Lu, S. Ruan, Y.-J. Zeng, *J. Mater. Sci.* **2018**, *53*, 16557–16566.
[33] O. Elbanna, M. Zhu, M. Fujitsuka, T. Majima, *ACS Catal.* **2019**, *9*, 3618–3626.
[34] M. Serrano-Ruiz, M. Caporali, A. Ienco, V. Piazza, S. Heun, M. Peruzzini, *Adv. Mater. Interfaces* **2016**, *3*,1500441–1500448.
[35] E. J. Popczun, C. G. Read, C. W. Roske, N. S. Lewis, R. E. Schaak, *Angew. Chem. Int. Ed.* **2014**, *53*, 5427–5430.
[36] M. Rezaee, S. M. M. Khoie, K. H. Liu, *CrystEngComm* **2011**, *13*, 5055–5061.
[37] E. P. Meagher, G. A. Lager, *Can. Mineral.* **1979**, *17*, 77–85.
[38] C. J. Howard, T. M. Sabine, F. Dickson, *Acta Crystallogr. Sect. B.* **1991**, *47*, 462–468.
[39] G. Tiouitchi, M. Ait Ali, A. Benyoussef, M. Hamedoun, A. Lachgar, M. Benaissa, A. Kara, A. Ennaoui, A. Mahmoud, F. Boschini, H. Oughaddou, A. El Kenz, O. Mounkachi, *Mater. Lett.* **2019**, *236*, 56–59.
[40] S. Peng, Y. Cao, F. Zhou, Z. Xu, Y. Li, *Appl. Surf. Sci.* **2019**, *487*, 315–321.
[41] E. Bonera, A. Molle, *Nanomaterials* **2022**, *12*, 1410–1418.
[42] Prathvi, S. A. Bhandarkar, A. Kompa, D. Kekuda, M. S. Murari, M. P. Telenkov, K. K. Nagaraja, M. K. Rao, *Surf. Interfaces* **2021**, *23*, 100910–100918.
[43] S. A. Bhandarkar, Prathvi, A. Kompa, M. S. Murari, D. Kekuda, M. K. Rao, *Opt. Mater.* **2021**, *118*, 111254–111261.
[44] S. Liang, M. Hasan, J.-H. Seo, *Nanomaterials* **2019**, *9*, 566–573.
[45] D. Wang, P. Yi, L. Wang, L. Zhang, H. Li, M. Lu, X. Xie, L. Huang, W. Huang, *Front. Chem.* **2019**, *7*, article 21.
[46] A. Favron, E. Gaufrès, F. Fossard, A.-L. Phaneuf-L'Heureux, N. Y.-W. Tang, P. L. Lévesque, A. Loiseau, R. Leonelli, S. Froncoeur, R. Martel, *Nat. Mater.* **2015**, *14*, 826–832.
[47] H. B. Ribeiro, M. A. Pimenta, C. J. S. De Matos, *J. Raman Spectrosc.* **2018**, *49*, 76–90.
[48] X. Li, L. Xiao, H. Wang, J. Song, Q. Xu, M. Ye, J. Xu, *Prog. Nat. Sci.:Mater.* **2023**, *33*, 100–107.
[49] L. Capozzoli, A. Caprì, V. Baglio, E. Berretti, C. Evangelisti, J. Filippi, I. Gatto, A. Lavacchi, M. Pagliaro, F. Vizza, *J. Power Sources* **2023**, *562*, 232747–232757.
[50] H. Kaur, S. Yadav, A. K. Srivastava, N. Singh, J. J. Schneider, O. P. Sinha, V. V. Agrawal, R. Srivastava, *Sci. Rep.* **2016**, *6*, 34095–34102.
[51] J. Zhang, K. Zhang, J. Yang, G.-H. Lee, J. Shin, V. W.-H. Lau, Y.-M. Kang, *Adv. Energy Mater.* **2018**, *8*, 1800283–1800292.
[52] N. Boonprakob, N. Wetchakun, S. Phanichphant, D. Waxler, P. Sherrell, A. Nattestad, J. Chen, B. Inceesungvorn, *J. Colloid Interface Sci.* **2014**, *417*, 402–409.
[53] M. Caporali, M. Serrano-Ruiz, F. Telesio, S. Heun, A. Verdini, A. Cossaro, M. Dalmiglio, A. Goldoni, M. Peruzzini, *Nanotechnology* **2020**, *31*, 275708–275718.
[54] S. Yang, G. Chen, A. G. Ricciardulli, P. Zhang, Z. Zhang, H. Shi, J. Ma, J. Zhang, P. W. M. Blom, X. Feng, *Angew. Chem. Int. Ed.* **2020**, *59*, 465–470.
[55] Q. Zhong, X. Pang, *J. Mater. Sci.* **2023**, *58*, 2068–2086.
[56] L. Su, X. Cui, T. He, L. Zeng, H. Tian, Y. Song, K. Qi, B. Y. Xia, *Chem. Sci.* **2019**,*10*, 2019–2024.
[57] Y. Yan, J. Huang, X. Wang, T. Gao, Y. Zhang, T. Yao, B. Song, *Front. Chem.* **2018**, *6*, 521–528.
[58] D. Reyes-Coronado, G. Rodriguez-Gattorno, M. E. Espinosa-Pesqueira, C. Cab, R. De Coss, G. Oskam, *Nanotechnology* **2008**, *19*, 145605–145614.
[59] M. Vanni, M. Serrano-Ruiz, J. Filippi, M. C. Salvatici, E. Fonda, M. Peruzzini, M. Caporali, *ChemPlusChem* **2023**, *88*, e202200457.
[60] W. Gao, X. Bai, F. Fan, Y. Zhou, C. Li, Z. Zou et al., *Chem. Commun.* **2020**, *56*, 7777–7780.
[61] J. Lin, Y. Liu, Y. Liu, C. Huang, W. Liu, X. Mi, D. Fan, F. Fan, H. Lu, X. Chen, *ChemSusChem.* **2019**, *12*, 961–967.
[62] C. Xu, P. Ravi Anusuyadevi, C. Aymonier, R. Luque, S. Marre, *Chem. Soc. Rev.* **2019**, *48*, 3868–3902.
[63] M. Kopf, N. Eckstein, D. Pfister, C. Grotz, I. Krüger, M. Greiwe, T. Hansen, H. Kolhmann, T. Nilges, *J. Cryst. Growth* **2014**, *405*, 6–10.
[64] R. Guan, L. Wang, D. Wang, K. Li, H. Tan, Y. Chen, X. Cheng, Z. Zhao, Q. Shang, Z. Sun, *Chem. Eng. J.* **2022**, *435*, 135138–135146.
[65] O. Elbanna, M. Zhu, M. Fujitsuka, T. Majima, *ACS Catal.* **2019**, *9*, 3618–3626.
[66] J. Wu, S. Huang, Z. Jin, J. Chen, L. Hu, Y. Long, J. Lu, S. Ruan, Y.-J. Zeng, *J. Mater. Sci.* **2018**, *53*, 16557–16566.
[67] B. Tian, B. Tian, B. Smith, M. C. Scott, R. Hua, Q. Lei, Y. Tian, *Nat. Commun.* **2018**, *9*, 1397.
[68] X. Zhu, T. Zhang, Z. Sun, H. Chen, J. Guan, X. Chen, H. Ji, P. Du, S. Yang, *Adv. Mater.* **2017**, *29*, 1605776.
[69] P. Vishnoi, U. Gupta, R. Pandey, C. N. R. Rao, *J. Mater. Chem. A* **2019**, *7*, 6631–6637.

Manuscript received: May 16, 2023
Revised manuscript received: June 28, 2023
Accepted manuscript online: July 17, 2023
Version of record online: August 4, 2023